bioRxiv preprint doi: https://doi.org/10.1101/2021.07.21.453212; this version posted July 21, 2021. The copyright holder for this preprint (which was not certified by peer review) is the author/funder, who has granted bioRxiv a license to display the preprint in perpetuity. It is made available under aCC-BY-ND 4.0 International license.

Emergence of growth and dormancy from a kinetic model of the *Escherichia coli* central carbon metabolism

Yusuke Himeoka[a,b] **and Namiko Mitarai**[b,1]

[a]Universal Biology Institute, University of Tokyo, 7-3-1 Hongo, Bunkyo-ku, Tokyo, Japan; [b]The Niels Bohr Institute, University of Copenhagen, Blegdamsvej 17, Copenhagen, 2100, Denmark

This manuscript was compiled on July 21, 2021

Physiological states of bacterial cells exhibit a wide spectrum of timescale. Under the nutrient-rich conditions, most of the cells in an isogenic bacterial population grow at certain rates, while a small subpopulation sometimes stays in a dormant state where the growth rates slow down by orders of magnitude. What is the origin of such heterogeneity of timescales? Here we addressed this question by studying the kinetic model of *Escherichia coli* central carbon metabolism including the dynamics of the energy currency molecules, which have often been ignored. We found that the model robustly exhibits both the growing- and the dormant state. In order to unveil the mechanism of distinct behaviours, we developed a recursive method to simplify the model without changing the qualitative feature of the dynamics. Analytical and numerical studies of the 2-variable minimal model revealed the necessary conditions for the distinct behaviour, namely, the depletion of energy due to the futile cycle and its non-uniform impact to the kinetics because of the coexistence of the energy currency-coupled and uncoupled reactions as well as branching of the network. The result is consistent with the experimental evidences of the appearance of the futile cycle in mutants and provides a possible explanation for the appearance of dormant cells that causes antibiotic persistence.

metabolism | persistence | dormancy | microbiology | dynamical systems

Bacterial growth rates span in a wide range of timescales: *Escherichia coli* cells typically double every 20 minutes under the nutrient-rich conditions (1) while it is reported that non-sporulating *Bacillus subtilis* showed 4-day doubling time (2), and the doubling times of some oceanic bacteria are estimated to be years (3). Interestingly, the growth rates of the cells in a single-cell level can be heterogeneous even in a clonal population growing at a constant rate (4–10). Further, a small fraction of the cells sometimes exhibit dormancy where the growth rate of such cells is slower than that of the other cells in the orders of magnitude. This phenotypic heterogeneity showing dormancy in the log phase is the main cause of the type-II persister (5, 11–13) that have high tolerance to antibiotics.

Where do the multiple timescales originate in the cellar dynamics? Several mechanisms for triggering dormancy and persistence have been proposed so far: studies discovered links between the expression of toxin-antitoxin modules and the persister fraction. The toxin is a protein that typically inhibits important cellular functions such as translation, and thus, it can slow down the cellular growth and trigger stress response mechanisms of the cells, increasing the persister fraction in some cases (14, 15). Aside from the toxin-antitoxin modules, the growth-modulating genetic circuits exhibiting bistability were found (16, 17). Also, the epigenetic "memory" by DNA modification in prokaryotes has recently been discussed in relation to the slow timescale of persister cells (18).

The above listed studies attribute the origin of the slow timescale to the gene expression patterns. Here in the present manuscript, we explored another possibility: the multiple timescales originated from the metabolic dynamics itself, without regulatory changes. Metabolic reaction networks are highly interconnected via cofactors such as ATPs, and thus, the kinetic models of metabolic networks should have high nonlinearities. The emergence of multiple timescales is one of the hallmarks of nonlinear dynamical systems. Indeed, the studies of simple catalytic reaction network showed that the relaxations to the steady-state are much slower than that inferred from the rate-constants of the reactions and exhibit multiple plateaux (19, 20). Thus, it is worth asking if the metabolic dynamics, by itself without regulations, lead to widely spanning timescales.

However, in the studies of *E.coli* metabolic dynamics, little research has been done to ascribe the origin of the multiple timescales of cellular growths to metabolic dynamics. Instead, most of the efforts have been devoted for the quantitative predictions of the metabolic dynamics under given experimental conditions (21–31). Interestingly, the kinetic models for such quantitative predictions have a common simplification style: the dynamics of the cofactors are neglected (21–31), or if included, only the steady-states are in the focus, and the relaxation dynamics of the models are not actually computed

Significance Statement

Bacterial cells can exhibit extremely slow growth or dormancy, even when the environment allows fast growth. It is a challenging question how the cellular metabolism can show such a long timescale even though it operates in much shorter timescales to grow quickly under favorable conditions. By simulating the kinetic model of *Escherichia coli* metabolism including the energy currency molecules, we found that the system robustly exhibits distinctively fast and slow dynamics. Through a systematic reduction of the original model, we derived a minimal model that exhibits both slow and fast dynamics. The analysis demonstrated that it is the robust feature of the network structure that includes the futile cycle, energy currency-coupled and uncoupled reactions, and branching.

Author contributions: Y.H and N.M designed research; Y.H and N.M performed research; Y.H analyzed data; and Y.H and N.M wrote the paper.

The authors declare no competing interest.

[1] To whom correspondence should be addressed. E-mail: mitarai@nbi.ku.dk

bioRxiv preprint doi: https://doi.org/10.1101/2021.07.21.453212; this version posted July 21, 2021. The copyright holder for this preprint (which was not certified by peer review) is the author/funder, who has granted bioRxiv a license to display the preprint in perpetuity. It is made available under aCC-BY-ND 4.0 International license.

(32–36). By such simplifications, we have possibly overlooked some aspects of the dynamics of cellular metabolism. Indeed, it is reported that a simple kinetic model of glycolysis exhibits anomalous relaxation behaviour when the energy currency molecules are introduced to the model (37).

Therefore, in the present manuscript, we study the kinetic model of *E.coli* central carbon metabolism including the dynamics of the cofactors. We show that the model robustly exhibits two distinct dynamics which are reminiscent of the exponentially growing- and dormant (or persister) cells, depending on the initial conditions. In order to derive the minimal reaction network showing qualitatively the same dynamics, we develop a recursive method to reduce the model variables. As a consequence of the model reduction, the minimal network is obtained consisting of five variables and six reactions. The analysis reveals two necessary conditions for the emergence of both growth and dormant dynamics.

Results

Model. In the present manuscript, we study the *E. coli* core network (38) as one of the simplest models of the real metabolic reaction networks. The *E. coli* core model was obtained from BiGG database (39). The model contains the stoichiometry and the reversibility of the reactions. The *E. coli* core model has 52 and 75 intracellular metabolites and reactions, respectively. After an appropriate data curation as described later, we implemented the model by using the ordinary differential equation (ODE) that describes dynamics of concentrations of metabolites.

We applied several modifications to the model to make it suitable for the ODE implementation. First, small molecules such as O_2, H_2O, and NH_4, were not considered as variables but treated as constants under the assumptions that the external concentration of these chemicals are kept constant and uptakes/secretions of them take place quickly. The uptake and secretion pathway of all carbon sources except glucose are removed.

Under the anaerobic conditions, cells transfer the free energy to ATP directly, while under the aerobic conditions, most of the energy transfer takes an indirect form: the energy is first transferred to other chemicals such as NADH and NADPH, and then, the stored energy in NADH, NADPH, and others are used for converting ADP to ATP. The conversion yield of ATP per NADH in the *E. coli* core model is 1.25* and NADH/NADPH yield is roughly unity. For introducing the cofactors to the model in a simple manner, we suppose that the energy transfers via NADH and NADPH are sufficiently fast and ATP/NADH(NAPDH) yield as unity. According to these assumptions, we replace NAD(NADP) and NADH(NADPH) by ADP and ATP, respectively (we discussed the validity of this assumption in the Discussion section and *SI text* Section.9). Full lists of the chemical components and the reactions are provided in *SI Data*.1.

Also, the stoichiometry of the growth reaction was modified. The original *E. coli* core model has the biomass production reaction leading to the cell growth consisting of 16 substrates and 7 products with non-integer stoichiometry constants. For the kinetic modeling, such reactions having too many substrates and products leads to numerical instability and non-integer stoichiometry is unreasonable. Thus, we replaced the biomass production reaction by a following reaction: (Erythrose 4-phosphate) + (L-Glutamine) + (ATP) → (ADP). This reaction is much simpler than the original one but requires the model to run all the modules of the metabolic reactions, namely pentose phosphate pathway for Erythrose 4-phosphate (e4p), TCA cycle for L-Glutamine (gln), and energy generation for ATP. Hereafter, we call this simplified biomass production reaction as the growth reaction.

The resulting model consists of 32 variables and 40 reactions. The final metabolic reaction network is drawn in Fig. 1. Our model cell takes up the nutrient from the node labeled as "glc" which has a constant concentration, performs successive conversion of the chemicals with generating energy, and proceeds the growth reaction.

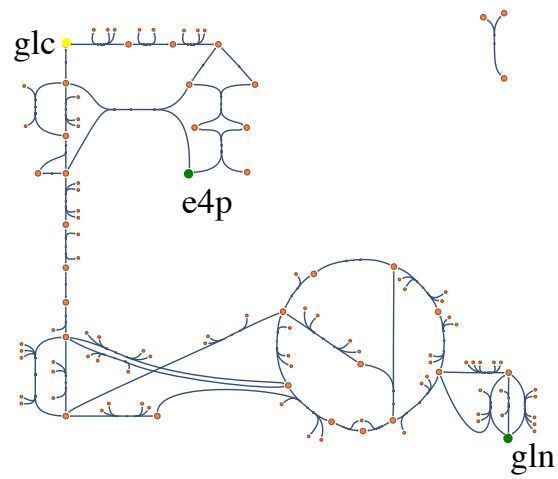

Fig. 1. The metabolic network of the *E. coli* core model generated by Escher (39). The sole carbon source (glucose-6-phosphate) is placed at the left top (abbreviated as glc). We highlighted the substrates of the growth reaction other than ATP, namely, e4p and gln. The growth reaction is not drawn.

First, we simulated the model with realistic setups. The kinetic parameters of *E. coli* core model have been estimated using the metabolic ensemble modeling (MEM) by Khodayari and colleagues (34). We derived Michaelis-Menten type rate equation for each reaction according to the enzyme kinetics used in (34) with the presented kinetic parameters. Then we assumed that each chemical species is consumed/synthesized by associated reactions, diluted as the cell grows, and spontaneously degraded at a slow rate. Thus, the temporal change of the concentration of the ith chemical species X_i is ruled by

$$\frac{d[X_i]}{dt} = \sum_j S_{ij} J_j - d[X_i] - \mu[X_i], \qquad [1]$$

where S is the stoichiomety matrix and J_i's are the fluxes due to chemical reactions. d and μ are the spontaneous degradation rate and the growth rate, respectively. Note that the concentrations of enzymes are supposed to be constant and lumped in the kinetic parameters. We assumed that the spontaneous degradation is very slow process and represented by a single parameter. The dilution and degradation terms are omitted in the equations of AMP, ADP, and ATP because de-novo synthesis of the adenine nucleotide carriers are not

*via NADH16, CYTB, and ATPS4r.

bioRxiv preprint doi: https://doi.org/10.1101/2021.07.21.453212; this version posted July 21, 2021. The copyright holder for this preprint (which was not certified by peer review) is the author/funder, who has granted bioRxiv a license to display the preprint in perpetuity. It is made available under aCC-BY-ND 4.0 International license.

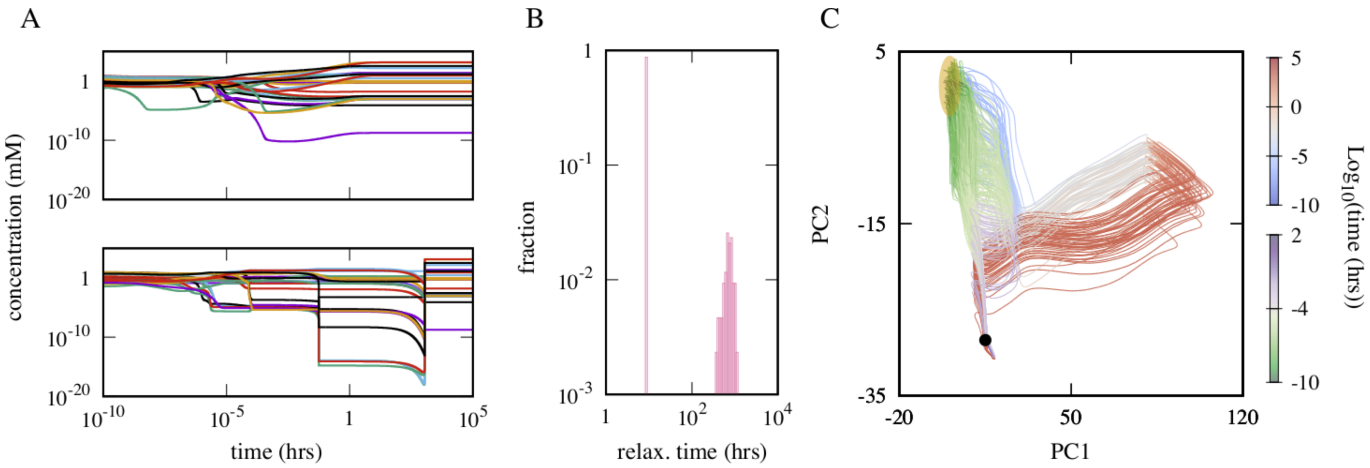

Fig. 2. A. Two characteristic dynamics of $E.\ coli$ core model starting from different initial points. While the growth rate of the cell is ≈ 0.5 per hour at the attractor, there are huge differences in the relaxation behaviours between the top and bottom panel. B. The distribution of the relaxation time showing a clear bimodality. C. Trajectories are overlaid in 2-dimensional principal component space. Color indicates $\log_{10}$ of time. The trajectories having shorter relaxation time (several hours) are colored in green-white-purple while the others are colored in blue-white-red. All initial points cluster at the region highlighted in orange and the black point corresponds to the attractor. Initial concentration of each metabolites is 10^u (mM) with u as a random number uniformly distributed in $[-1, 1]$ while the total concentrations of adenine nucleotide carriers are normalized. Parameters other than ones obtained from (34) are $[\mathrm{glc}] = 20$(mM),$A_t = 1$(mM),$d = 5 \times 10^{-3}$(hour^{-1}), $v_g = 3.6 \times 10^4$(mM$^{-2}\cdot$ sec^{-1}) and $r = 5.0$(mM^{-1}).

modelled in the *E. coli* core model. This assumption is equivalent to suppose the homeostasis of the total adenine nucleotide carriers. (Later we check that the assumption can be relaxed by introducing a phenomenological reaction for de-novo synthesis of AMP). According to the growth reaction which we have introduced above, our model cell grows as the reaction (Erythrose 4-phosphate) + (L-Glutamine) + (ATP) $\rightarrow$ (ADP) proceeds. We chose the simplest kinetics of the growth reaction given by $J_g = v_g[\mathrm{e4p}][\mathrm{gln}][\mathrm{atp}]$ and the growth rate as $\mu = rJ_g$. We fit the values v_g and r so that the growth rate at the steady state is in the range of the typical growth rate of *E. coli* in minimal glucose media, in the order of 0.1 per hour, and set the spontaneous degradation rate d as approximately one-hundredth of it. The concentration of the nutrient ([glc]) and the total concentration of the adenine nucleotide carriers (A_t) are set to 20mM and 1mM, respectibely (see *SI Text* Section.1).

Dormant trajectory. We computed the dynamics of the *E. coli* core model from randomly chosen initial concentrations. The initial concentration of each chemical is given by 10^u with u as a random number uniformly distributed in $[-1, 1]$ while the concentrations of ATP, ADP, and AMP are normalised so that the total concentration is identical for all the initial conditions. We found that the model exhibited two qualitatively distinct relaxation behaviours depending on the initial conditions. The typical time course of each type is plotted in Figs. 2 A in log scale, to depict the wide range of the concentration and timescale. Even though the two trajectories eventually relax to the same attractor, the relaxation behaviours are evidently distinct. First, the concentrations after milliseconds ($\sim 10^{-5}$ hours) are different between the top and bottom panel in many orders of magnitude. Furthermore, the characteristic timescale between them is clearly different. The concentrations of the chemicals reach close to the steady values in seconds in the top panel, while the concentrations keep changing for a much longer time, $t \approx 10^3$ hours in the bottom panel. When sampled over various initial conditions, the distribution of the relaxation time has a clear bimodality as shown in Fig. 2B. Here, the relaxation time is defined as the time when the distance between the attractor and the state in the logarithm-converted phase space first becomes less than 0.05.

For visualising the differences among the trajectories, we analysed all the trajectories in the phase space by the principal component analysis (PCA, see Materials and Methods) where all the trajectories are converted to the logarithmic scale. We plotted all trajectories projected onto the 2-dimensional principal component space (PCS) in Fig. 2C. The trajectories were classified into two groups by the relaxation time and differently colored. The first group is quickly-relaxing trajectories that the trajectory in the top panel of Fig. 2A belongs to (colored in green-white-purple). The trajectory in the bottom panel of Fig. 2A is grouped into the other group, colored by blue-white-red which takes much longer time to relax to the attractor. Interestingly, the two groups of the trajectories are different not only in the relaxation time, but also in the shape of the trajectory in the PC1-PC2 space. Note that, the initial position of the two classes of trajectories (highlighted in oragne) are not clearly separated in the PC1-PC2 space.

The remarkable gaps between the timescale of chemical reactions, and accordingly, the growth rate during their relaxations highlight the difference between two time courses. The specific growth rate μ at the attractor is ≈ 0.5 hour^{-1} and the model cell achieves this growth rate in few seconds in the top panel of Figs. 2A, while less than 10^{-10} hour^{-1} in the bottom panel at $t = 10^2$ hours (at plateau). Thus, in the following sections, we call the trajectories of the second group "dormant trajectories" because of its extremely slower growth rate than the other group. Accordingly, the trajectories of the first group are termed as "growth trajectories". The following sections are devoted to unveiling the mechanism leading to the differentiation of the growth and dormant trajectories.

Simplification of reaction kinetics. The kinetic *E. coli* core model is, as it is, too complicated to understand the mechanism that leads to the two distinct relaxation trajectories. Thus, we

bioRxiv preprint doi: https://doi.org/10.1101/2021.07.21.453212; this version posted July 21, 2021. The copyright holder for this preprint (which was not certified by peer review) is the author/funder, who has granted bioRxiv a license to display the preprint in perpetuity. It is made available under aCC-BY-ND 4.0 International license.

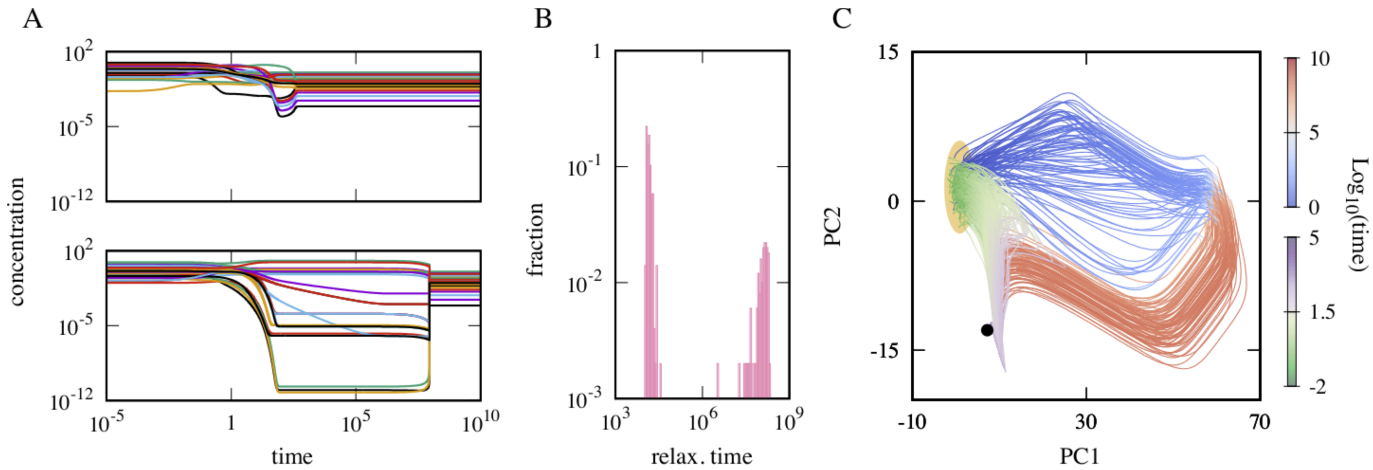

Fig. 3. A. Two characteristic dynamics of model0 starting from different initial points. The relaxation behaviours are qualitatively different between the top- and bottom panels. B. The distribution of the relaxation time showing a clear bimodality. C. Trajectories are overlaid in 2-dimensional principal component space. Color indicates $\log_{10}$ of time. The trajectories having shorter relaxation time (top panel of A) are colored in green-white-purple while the others are colored in blue-white-red. All initial points cluster at the region highlighted in orange and the black point corresponds to the attractor. Initial concentration of each metabolites is 10^u with u as a random number uniformly distributed in $[-1, 1]$ while the total concentrations of adenine nucleotide carriers are normalized. $v = 1$ and $\kappa = 10^{-6}$ for all reactions. Other parameters are $[\mathrm{glc}] = 1, A_t = 1, r = 0.1$ and $d = 10^{-8}$.

simplified the *E. coli* core model as follows. First, we modified the kinetics of the chemical reactions from the Michaelis-Menten formula to the mass-action rate equation. The rate of the ith chemical reaction $A \rightleftharpoons B$, J_i which was given by

$$J_i = v_i \frac{[A] - k_i[B]}{1 + [A]/K_A^{(i)} + [B]/K_B^{(i)}} \qquad [2]$$

is replaced by

$$J_i = v_i([A] - k_i[B]), \qquad [3]$$

where v_i and $v_i k_i$ are the rate constant of forward- and backward reaction, respectively. Note that the mass-action kinetics (Eq.[3]) is a special form of the Michaelis-Menten kinetics (Eq.[2]) in the parameter region where $[A] \ll K_A^{(i)}$ and $[B] \ll K_B^{(i)}$ hold (for general arguments, see (40)). We further simplified the rate equations by setting v_i's to unity and binarising k_i's for all i's. The *E. coli* core model contains the information of irreversibility for each reaction, and thus, if the ith reaction is reversible, we set k_i as unity, and otherwise, set it to $\kappa \ll 1$. We term this simplified version of the kinetic *E. coli* core model as model0 with an index for the following model reduction steps.

Surprisingly, the emergence of distinct relaxation trajectories is robust to such an extensive modification of the model. Figs. 3 are obtained from model0. While time courses, especially that of the dormant trajectory, become much smoother, the qualitative difference of the trajectories (Figs. 3A), bimodality of the distribution of the relaxation time (Fig. 3B), and the distinction of the trajectories in the PC1-PC2 space (Fig. 3C) were unchanged. This robustness implies that the emergence of the distinct trajectories stems from the structure of the metabolic reaction network of the *E. coli* core model, rather than choices of specific parameter values. Indeed, we confirmed that the distinct trajectories emerge if the kinetic parameters are randomly assigned instead of setting them unity (see *SI Text* Section.11).

Now it is worth asking, if there are understandably simple, minimal network architecture(s) in the *E. coli* core network which leads to the distinct trajectories. For extracting the architectures, we develop a method of systematic network reduction in the following section.

Systematic Model Reduction. In the present section, we reduce the *E. coli* core network by simply removing few chemical reactions step by step because we expect that most of the reactions are not vital for the emergence of the distinct trajectories. As illustrated in Fig. 4A, there are two types of reaction removal, namely, the simple removal and the contraction. First we describe the simple removal. Suppose that there are reactions $A \rightleftharpoons B$, $B \rightleftharpoons C$ and $C \rightleftharpoons A$, and also A and B are connected to the rest part of the network by the other reactions (Fig. 4A-(i)). The simple removal removes the reaction $B \rightleftharpoons C$ and $C \rightleftharpoons A$, and accordingly, eliminate the chemical C because it is a disconnected component in the network. In the contrast, chemical species are merged by the contraction (Fig. 4A-(ii)). It removes a reaction $A \rightleftharpoons E$, and then, the chemical A and E are identified forming a new chemical Æ. Here, we avoided the appearance of the dead-end chemical which has only one reaction because networks with dead-end chemicals can cause the heavy accumulation of the chemicals and it potentially leads to an artifactual anomalous relaxation behaviour. If the simple removal of a reaction results in the dead-end chemical(s), a few additional reactions are removed at the same time to avoid the dead-end chemical(s). A detailed algorithm for the network reduction is described in *SI Text* Section.2.

At each reduction step, we checked if the reduced model exhibits the two distinct classes of trajectories by computing its dynamics from randomly generated 512 initial points. First we used the bimodality of the relaxation time distribution as a criterion of the distinct trajectories. However, we found in some cases that the bimodality was unclear even though there were clearly different types of trajectories when we plotted the time courses and performed PCA. This is because the growth rate during the relaxation of both types of trajectories (growth and dormant) becomes smaller than the spontaneous

DRAFT

bioRxiv preprint doi: https://doi.org/10.1101/2021.07.21.453212; this version posted July 21, 2021. The copyright holder for this preprint (which was not certified by peer review) is the author/funder, who has granted bioRxiv a license to display the preprint in perpetuity. It is made available under aCC-BY-ND 4.0 International license.

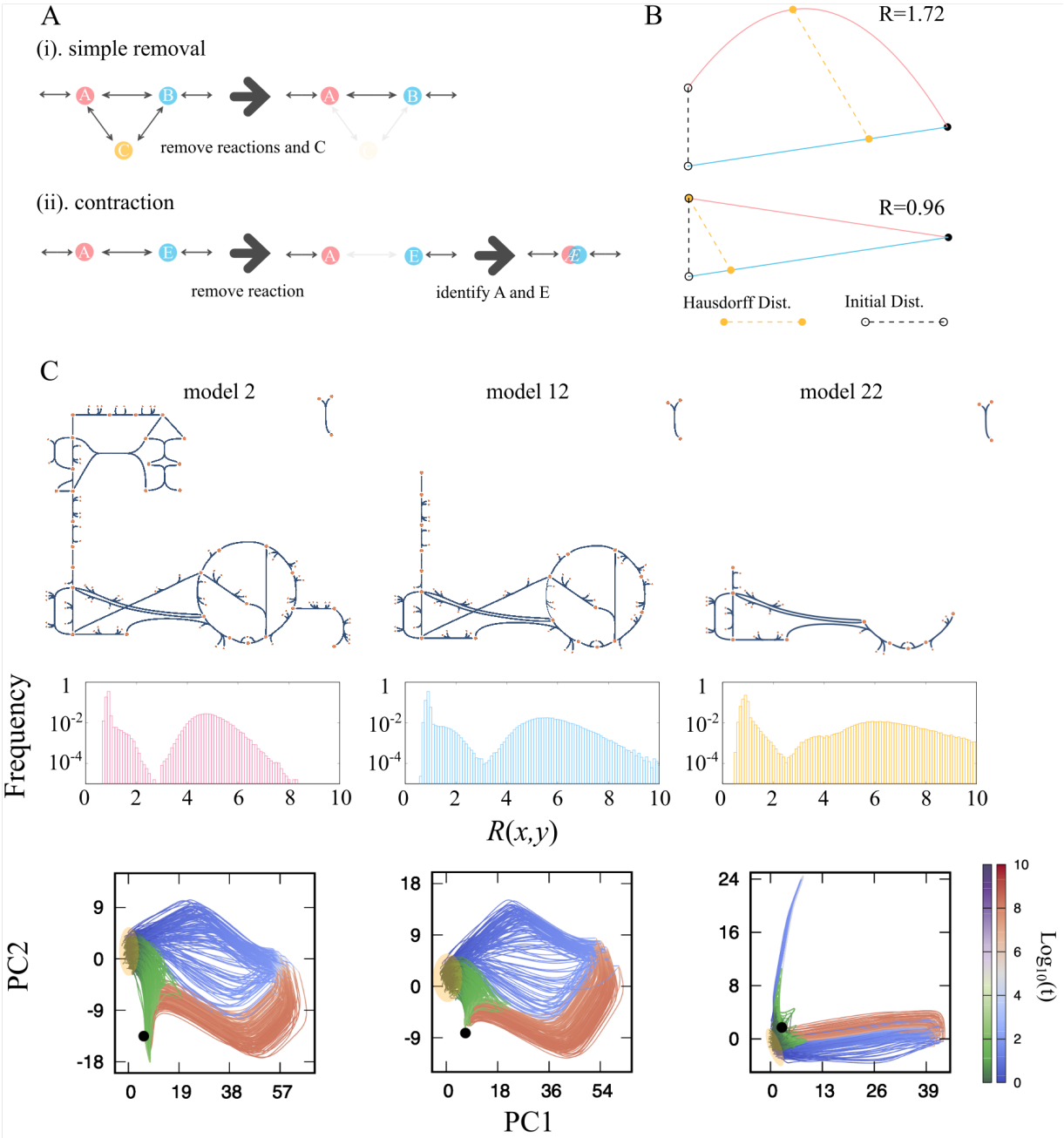

Fig. 4. A. Two types of reaction removal. The simple removal (top) just removes one or a few reactions from the network. The number of the reaction to be removed is determined so that the dead-end chemicals are not made by the removal. The contraction removes a single reaction first, and then, the substrate and product of the removed reaction are identified and regarded as a new chemical species. B. Illustrative description of the Hausdorff distance and the expansion ratio. There are two cases are depicted: the case with $R > 1$ (top) and $R < 1$ (bottom). The two lines (pink and cyan) are trajectories starting from the initial point of each (back circles), converging to the same attractor (black dot). The length of the yellow dashed line and the black dashed line give the Hausdorff distance and the initial distance, respectively. If one trajectory (pink) goes away from the other (blue), typically the Hausdorff distance becomes larger than the initial distance. In the contrast, in the case that the two trajectories approach each other, the Hausdorff distance is smaller than the initial distance. Note that the information of time is discarded in the argument. C. The reduced networks of the intermediate models (model 5, 15, and 25) are drawn. The sole nutrient (glucose) is at the left top corner of the network while the substrate(s) of the growth reaction except ATP are colored in yellow ((e4p,gln), akg, and icit for model 5, 15, and 25, respectively.). The distribution of the expansion ratio and the trajectories projected onto the PCS of each model are also plotted. The areas in each panel are the region where the initial points cluster. For the coloring protocol of the trajectories, see the main text.

bioRxiv preprint doi: https://doi.org/10.1101/2021.07.21.453212; this version posted July 21, 2021. The copyright holder for this preprint (which was not certified by peer review) is the author/funder, who has granted bioRxiv a license to display the preprint in perpetuity. It is made available under aCC-BY-ND 4.0 International license.

degradation rate d, and thus, the relaxation time of all the trajectories becomes approximately $1/d$ [†]. Thus, we decided to focus on the similarity of the trajectories instead of the relaxation time itself. In the following few paragraphs, we first intuitively explain how we quantify the similarity of the trajectories, and then, introduce the actual measure.

Suppose that an ODE model has a single attractor. Then, all the trajectories starting from different initial points eventually converge. We like to categorize the trajectories into different groups in a way that, if a pair of trajectories monotonically approach each other as they converge to the attractor, they belong to the same group. One may naïvely expect that we can state that two trajectories $x(t)$ and $y(t)$ monotonically approach each other if the Euclidean distance between them at the same time point, $d(x(t), y(t))$, is a monotonically decreasing function of t. However, since the initial points are distributed in the phase space, measuring the distance between the points on two trajectories at the same time point is unreasonable. Thus, instead of adopting this naïve definition of the monotonicity, we measure the maximum Euclidean distance between two trajectories in the phase space. It is known as the Hausdorff distance of the trajectories, given by

$$d_H(x, y) = \max\{\max_t \min_s d(x(t), y(s)), \max_t \min_s d(x(s), y(t))\}. \quad [4]$$

The Hausdorff distance first looks for the closest point of the trajectory y from the point $x(t)$, $y(s^*(t))$, and then find the pair of the points $(x(t), y(s^*(t)))$ which gives the maximum Euclidean distance. The same is done from the points of $y(t)$ and the larger value is chosen for the symmetry $d_H(x, y) = d_H(y, x)$. The Hausdorff distance thus measures how far the two trajectories are distant while trivially distant pairs of points are not taken into account (for example, the initial point of x and the endpoint of y, i.e, the attractor).

We cannot judge whether the trajectories go away from each other or not directly from the Hausdorff distance since it needs to be compared with the initial separation. Thus, we normalize the Hausdorff distance by the Euclidean distance between the initial points, $d(x(0), y(0))$ leading to

$$R(x, y) = \frac{d_H(x, y)}{d(x(0), y(0))}. \quad [5]$$

We call this ratio $R(x, y)$ as the expansion ratio of the trajectories x and y. It measures how much the initial distance has expanded. If $d_H(x, y)$ is smaller than the initial distance, $R(x, y)$ is less than unity[‡]. $R(x, y) > 1$ means that two trajectories go away from each other at least once despite they eventually converge to the same attractor. The concept of the Hausdorff distance and the expansion ratio are illustrated in Fig. 4B. Note that in this manuscript, the Euclidean distance, and accordingly, the Hausdorff distance are measured in the original high-dimensional phase space after applying the logarithm-conversion of the variables, not in the lower-dimensional principal component space.

The distribution is expected to have a trivial peak around $R = 1$. If the distribution has only a trivial peak, it indicates that all the trajectories are monotonically attracted to a single predominant stream in the phase space reaching the attractor. Oppositely, if the distribution has a non-trivial peak(s), then it means that the correlation between the initial distance and the Hausdorff distance is not simply scaled to each other. Therefore, in the present manuscript, we utilize the multimodality of the distribution of the expansion ratio as the criterion of the distinct trajectories (examples can be found in Fig. 4C). We judged the multimodality by fitting the distribution by a sum of Gaussian functions (see *SI Text* section.2). Note that in the following analysis, the computation of the expansion ratio and PCA were performed for the trajectories converted to the logarithmic scale so that the dynamic behaviours of the chemicals with low concentrations are also reflected to the analysis[§].

A Minimal Model. We have reduced the *E. coli* core model step-by-step according to the model reduction method described in the previous section. For accomplishing the network reduction, we manually determined the order of the reaction removal so that subsystems of the network are removed or contracted in consecutive reduction steps. We completed the model reduction by removing and contracting the L-glutamine synthesis pathway (4 steps), pentose-phosphate pathway (4 steps), glycolytic pathway (8 steps), and TCA cycle (12 steps) with the indicated number of steps in the parenthesis. The full list of the removed reactions is provided in *SI Data*.1. Also, the distributions of the expansion ratio and the trajectories on PCS of all the models are shown in *SI Text* Section.3. We also tried the model reduction in random orders of the reaction removal (see *SI Text* Section.10).

The reaction network, the distribution of the expansion ratio, and the trajectories projected onto the PCS of selected models are shown in Figs. 4C. The distributions of the expansion ratio show clear bimodality. We colored the trajectories based on the relaxation time of each. The figure shows that dormant trajectories (blue-white-red trajectories) commonly take detour ways to reach the attractor in the PCS. This is not an artifact due to the PCA. We computed the ratio of the line integral of the trajectory (L) to the Euclidean distance between the initial point and the attractor (D) in the original high-dimensional phase space for each trajectory. The average L/D ratio of the dormant trajectories was indeed bigger than that of the growth trajectories (*SI Text* Section.5). We found only the 10th model showed bistability (all the other models are monostable). While in the analysis, we chose the trajectories relaxing to the major attractor that approximately 92% of the initial points converge to, the trajectories relaxing to the minor attractor also showed the bimodal distribution of the expansion ratio and a clear distinction of the trajectories on PC1-PC2 space (see *SI Text* Section.6)

After the 28 steps of reductions, we reached the stage that no more reduction is possible without losing the multimodality of the distribution of the expansion ratio. The reaction network and reaction names remained in this minimal network (model 28) are depicted together with the original *E. coli* core network in Fig. 5A. The network consists of glucose (glc), phosphoenolpyruvate (pep), pyruvate (pyr), oxaloacetate (oaa), ATP, ADP, and AMP. As highlighted in the original network, the reaction from glc to pep is the contraction of the

[†] In principle, we can overcome this problem by setting d to be sufficiently small such as 10^{-20}. However, it requires ridiculous amounts of computation. The distributions of the relaxation time for all the models in the reduction step are presented in *SI Text* Section.3

[‡] R becomes smaller than 1 if there is any point on x which is closer to $y(0)$ than $x(0)$. This argument is symmetric for the swap of the indices.

[§] As a side effect of the logarithm-conversion, the behaviours of the chemicals with quite low concentrations may be too much highlighted. We computed the expansion ratio with cut-offs of the concentrations for a lower-side, see *SI Text* section.4

DRAFT

bioRxiv preprint doi: https://doi.org/10.1101/2021.07.21.453212; this version posted July 21, 2021. The copyright holder for this preprint (which was not certified by peer review) is the author/funder, who has granted bioRxiv a license to display the preprint in perpetuity. It is made available under aCC-BY-ND 4.0 International license.

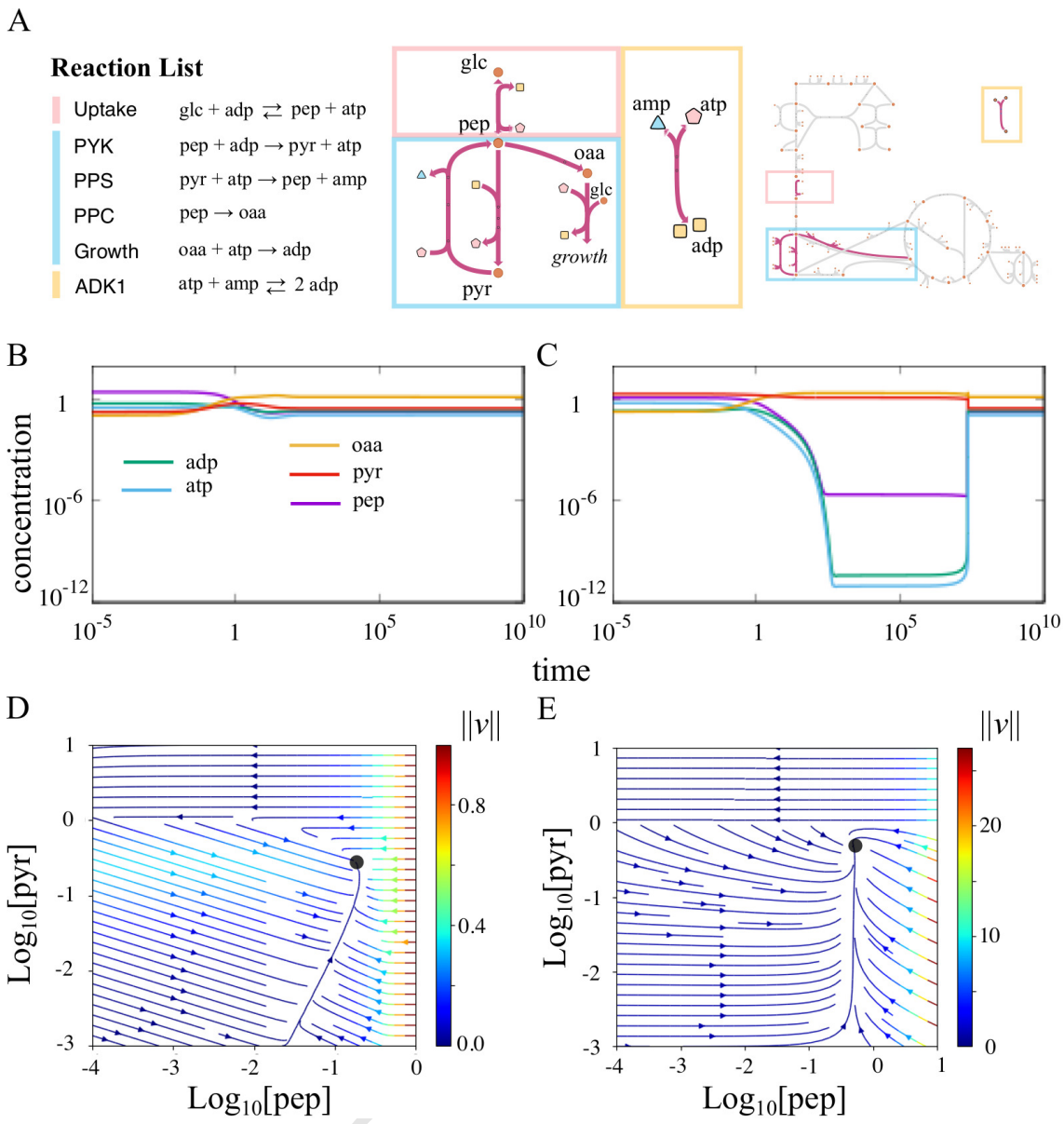

Fig. 5. A. The list of the reactions in the minimal network (left). The structure of the minimal network (middle). The original network with the reactions in the minimal model is highlighted (right). The minimal model consists of three parts, namely, the glycolytic pathway (pink bar and boxes), the joint part between the glycolytic pathway and the TCA cycle (cyan bar and boxes), and the adenosine kinase reaction (yellow bar and boxes). B and C. Example time courses of the growth trajectory (B) and the dormant trajectory (C) of the minimal model. D. The streamline representation of the vector field of the 2-variable minimal model where the steady values of $[\mathrm{atp}]$, $[\mathrm{adp}]$ and $[\mathrm{oaa}]$ under given $[\mathrm{pep}]$ and $[\mathrm{pyr}]$ are numerically solved. E. The streamline representation of the simplified minimal model. Color indicates the norm of the vector $v = (d[\mathrm{pep}]/dt, d[\mathrm{pyr}]/dt)$ at each point and the black dots indicate the attractor of each in D and E. $\phi_0 = 10^{-8}$ in E.

glycolytic pathway and oaa is representative of the chemicals in the TCA cycle. It is worth noting that the local structure of the network among pep, pyr, and oaa are unchanged (cyan boxes). Therefore, the minimal network is obtained by removing the pentose phosphate pathway and contracting the glycolytic pathway and the TCA cycle. Also, the reaction ADK1 converting two ADPs to ATP and AMP is conserved. As shown in Fig. 5B and C, the model still exhibits the distinct trajectories.

The model consists of five variables (recall that [glc] and $[\mathrm{atp}] + [\mathrm{adp}] + [\mathrm{amp}]$ are constant). In order to simplify the model further, we adiabatically solved the concentrations of three chemicals, [atp], [adp], and [oaa], under given values of [pep] and [pyr] to eliminate these variables from the model. This adiabatic elimination of the three variables does not violate the multimodality of the distribution of the expansion ratio. The set of ODEs of the minimal model is then given by

bioRxiv preprint doi: https://doi.org/10.1101/2021.07.21.453212; this version posted July 21, 2021. The copyright holder for this preprint (which was not certified by peer review) is the author/funder, who has granted bioRxiv a license to display the preprint in perpetuity. It is made available under aCC-BY-ND 4.0 International license.

$$\begin{aligned}\frac{d[\mathrm{pep}]}{dt} &= -([\mathrm{atp}][\mathrm{pep}]-[\mathrm{adp}][\mathrm{glc}])\\ &- ([\mathrm{pep}]-\kappa[\mathrm{oaa}])+([\mathrm{atp}][\mathrm{pyr}]-\kappa[\mathrm{amp}][\mathrm{pep}])\\ &- ([\mathrm{adp}][\mathrm{pep}]-\kappa[\mathrm{atp}][\mathrm{pyr}])\\ &- (d+r[\mathrm{oaa}][\mathrm{atp}])[\mathrm{pep}], \qquad [6]\\ \frac{d[\mathrm{pyr}]}{dt} &= -([\mathrm{atp}][\mathrm{pyr}]-\kappa[\mathrm{amp}][\mathrm{pep}])\\ &+ ([\mathrm{adp}][\mathrm{pep}]-\kappa[\mathrm{atp}][\mathrm{pyr}])\\ &- (d+r[\mathrm{oaa}][\mathrm{atp}])[\mathrm{pyr}], \qquad [7]\end{aligned}$$

where [atp], [adp] (accordingly [amp]), and [oaa] are adiabatically solved, and thus, are the functions of [pep] and [pyr].

The two-variable system allows us to visualize the vector field. As shown in Fig. 5D, interestingly, there is a boundary below and above which the streamlines change the direction dramatically ([pep] $\lesssim 0.1$ and [pyr] ≈ 1). Below the boundary, the state relaxes to the attractor rather straightforwardly corresponding to the dynamics shown in Fig. 5B (growth trajectory). On the other hand, trajectories starting from the upper region first travel to the left side of the phase space (small [pep] region) and return back to the attractor, corresponding to Fig. 5C (dormant trajectory). We attribute the emergence of the distinct trajectories to this dramatic change of the directions of the vector field occurring across the boundary. Hereafter, we call the region above- and below the boundary as the dormant and the growth region, respectively.

Conditions for the emergence of distinct trajectories. What determines the boundary between the growth- and the dormant region, and why is the vector field of the 2-variable model (Fig. 5D) almost parallel to the horizontal axis in the dormant region? For the first point, we found that there are large gaps of the concentrations of ATP and ADP between the two regions. In the dormant region, their concentrations are low ($\sim 10^{-8}$) while the growth region, they are in the order of 0.1. This gives an insight for the second point. We found that the drastic change of the direction of the vector field occurs because four of the five reactions of the model couple with the adenine nucleotide carriers, and thus, these reactions almost completely halt in the dormant region.

Intuitively, the low level of ATP and ADP in the dormant region can be understood from the reactions in Fig. 5A as follows. First, let us consider the situation where the concentrations of pep and pyr are in the dormant region. If in addition the concentration of pep is low, the uptake reaction proceeds the direction glc+adp→pep+atp. When this reaction accumlates some ATP, PPS proceeds in the direction pyr+atp→pep+amp, because the concentration of pep is low. In total, the uptake reaction and PPS form a futile cycle that converts ATP and ADP into AMP. Note that the PPS does not easily results in accumulation of pep, because of PPC reaction. If the concentration of pep is high but pyr is also high that the system is still in the dormant region, PYK plays the same role of the uptake reaction in the previous case. Thus, a futile cycle converting ATP and ADP into AMP is formed in both cases. If the conversion from ATP and ADP into AMP is slow enough, the other reaction, ADK1 (atp+amp⇌2ADP) proceeds to balance [atp] + [adp] and [amp]. However, ADK1 cannot balance them if the conversion is too fast because the reaction needs ATP.

Indeed, this intuitive description is consistent with the analytical estimate of the boundary. For that, we derive the boundary between the growth and dormant region for [pep] $\ll 1$. The boundary is given by the concentration of pyr leading to a low concentration of ATP and ADP with a given value of [pep]. For the estimation of the critical [pyr], we sum up $d[\mathrm{atp}]/dt$ and $d[\mathrm{adp}]/dt$ and assume [atp], [adp], [pep] $= O(\epsilon)$ with $\epsilon \ll 1$. Also, recall that the irreversibility parameter κ in (Eq. 6) is small. Then we obtain

$$\frac{d([\mathrm{atp}]+[\mathrm{adp}])}{dt} = J_{\mathrm{ADK1}} - J_{\mathrm{PPS}} \sim [\mathrm{atp}](v_{\mathrm{ADK1}}A_t - v_{\mathrm{PPS}}[\mathrm{pyr}]), \qquad [8]$$

where we explicitly write down the rate parameter v_*'s and the total concentration of adenine nucleotide carriers A_t for the interpretation of the estimate. If the first term of the right most side is larger than the second term, [atp]+[adp] increases, while in the opposite situation the sum keeps decreasing to zero as long as [atp] is non-zero. This shift occurs at $v_{\mathrm{PPS}}[\mathrm{pyr}] \sim v_{\mathrm{ADK1}}A_t$, and it gives the boundary between the growing and the dormant regions.

Next, we explain how the decrease of [atp] and [adp] leads to the vector field parallel to the horizontal axis in the dormant region (Fig. 5D). Let us assume that the concentrations of ATP and ADP are approximately the same and well-represented by a single lumped parameter ϕ. Also, for a simplicity, we set the irreversibility parameter κ to zero. Then, the ODE for the 2-variable minimal model (Eq. 6) is given by

$$\begin{aligned}\frac{d[\mathrm{pep}]}{dt} &= \phi(1-[\mathrm{pep}]+[\mathrm{pyr}]+r[\mathrm{oaa}])-(1+d)[\mathrm{pep}], \qquad [9]\\ \frac{d[\mathrm{pyr}]}{dt} &= \phi([\mathrm{pep}]-[\mathrm{pyr}]+r[\mathrm{oaa}])-d[\mathrm{pyr}], \qquad [10]\end{aligned}$$

where [oaa] is the function of ϕ, while it becomes constant as ϕ approaches 0. From the equation, we can see that if the concentration of ATP and ADP, represented by ϕ, is $O(1)$ (i.e, in the growth region), the timescale of the system is $O(1)$. On the other hand, if ATP and ADP deplete and $\phi \approx 0$ holds in the dormant region, the timescale of $d[\mathrm{pyr}]/dt$ becomes $O(d)$. Since the spontaneous degradation rate d is sufficiently smaller than unity, $|d[\mathrm{pep}]/dt| \gg |d[\mathrm{pyr}]/dt|$ holds, and it leads to the vector field being almost parallel to the [pep] axis as depicted in Fig. 5D.

To confirm if the simplification above still captures the feature of the vector filed in Fig. 5D, we have drawn the vector field of the simplified model Eq.[9] and [10] with $\phi = \max\{1-[\mathrm{pyr}], \phi_0\}$ in Fig. 5E. It well captures the feature of the original vector field. We have confirmed that the shape of the vector field is robust to the choice of the function ϕ. Also, we analytically solved the model without the growth dilution term (Eq.[9] and [10] with $r = 0$) and found that the model has only a single timescale which is $O(1)$ in the growth region (see *SI Text* Section.7).

The simplified model (Eq.[9] and [10]) highlights that the timescale of $d[\mathrm{pep}]/dt$ is much faster than that of $d[\mathrm{pyr}]/dt$ in the dormant region. The right hand side of Eq.[9] has the term $(1+d)[\mathrm{pep}]$, while that in Eq.[10] is only the degradation term $d[\mathrm{pyr}]$, and this difference results in the parallel streamline in the phase space (Fig. 5E). It is worth noting where the term $(1+d)[\mathrm{pep}]$ in Eq.[9] comes from. d corresponds to the constant-rate degradation term, and the reactions coupled with either ATP or ADP should have the rate being proportional

DRAFT

bioRxiv preprint doi: https://doi.org/10.1101/2021.07.21.453212; this version posted July 21, 2021. The copyright holder for this preprint (which was not certified by peer review) is the author/funder, who has granted bioRxiv a license to display the preprint in perpetuity. It is made available under aCC-BY-ND 4.0 International license.

to ϕ. Therefore, this timescale 1 comes from the reaction coupled neither with ATP nor ADP, namely, PPC (pep→oaa). All the reactions except PPC are coupled with either ATP or ADP, and thus, the reactions slow down over the boundary between the growth- and the dormant region. However, the rate of PPC has no direct effect from the depletion of ATP and ADP. Then, even after the slowing down of almost all reactions, pep is kept being consumed, and it leads to the characteristic dynamics of the dormant trajectory.

Note that, if PPC were also coupled with ATP and ADP, $(1+d)[\mathrm{pep}]$ term in Eq.[9] would have been replaced by $(\phi + d)[\mathrm{pep}]$. In such a case, all the reactions would have been uniformly slowed down by the depletion of ATP and ADP, and the direction of the vector field would not change over the boundary as drastically as Fig. 5D. Thus, it is vital that the reaction system partially slows down due to the depletion of ATP and ADP.

It is noteworthy that the network structure is also a part of the mechanism: if PPC were the reaction converting pyr to oaa instead of pep to oaa, the drastic change of the direction of the vector field as Fig.5D would not be resulted. If PPC were pyr → oaa, the main part of the reaction network (reactions except ADK1) would have no branch. The slowing down of the upstream reactions of PPC (i.e, uptake, PYK, and PPS) would be rate-limiting steps of it and PPC would slow down coordinated with these reactions.

The above two points may suggest that large discrepancies of the chemical concentrations between the steady-state and the plateaux lead to distinct dynamics. In both cases–PPC with energy coupling and the main network without a branch–the reactions uniformly slow down. In such scenarios, even if ATP and ADP deplete, the difference between production and consumption of each chemical stay relatively small, and thus, the changes of the concentrations remain small. However, if the slowing-down occurs heterogeneously on the network, some chemicals will have a large mismatch between the production and the consumption. As a consequence, the concentrations of such chemicals drastically change from the concentrations before the depletion of ATP and ADP.

To sum up, the mechanism of the emergence of the distinct trajectories has two parts: (i) the unbalance of energy (ATP and ADP) production and consumption, and (ii) partial slowing-down of the reaction system caused by non-uniform coupling to the energy currencies and branching of the network.

Discussion. We have shown that *E.coli* central carbon metabolism exhibits distinctly different dynamics depending on the initial conditions. The two types of trajectories greatly differed in terms of the relaxation time and the growth rate during the relaxation, and thus, we termed them as the growth- and the dormant trajectories. We developed a systematic method to simplify the reaction network without losing the distinct trajectories. By the successive reduction of the model, we eventually reached the minimal network still exhibiting the qualitatively same behavior.

By drawing the vector field of the 2-variable minimal model, we found that there is a boundary at which the vector field changes the direction drastically. Indeed, the two regions are divided by the boundary corresponding to the set of the initial points of the growth- and the dormant trajectories. Analysis led that there are at least two vital requirements for the distinct trajectories: (i) the unbalance of the energy production and consumption and (ii) the partial slowing-down of the reactions due to the non-uniform coupling with the energy currency molecules and branching of the network.

To confirm if the requirements are not limited to the specific model reduction example, we performed the reaction removal for the model reduction in 16 different randomized orders. All the minimal networks obtained by the random reduction were larger than that derived in the result section. However, the models share two features: (a) the models keep ADK1 reaction and AMP (note that it is possible to eliminate AMP from the model), and (b) in each networks, there are both reactions, with- and without the coupling to the energy currency molecules (ATP, ADP and AMP) as well as branches. The shared features correspond to the requirements above. We also found that the total concentration of ATP and ADP plays a central role in the emergence of distinct trajectories. If $[\mathrm{atp}]+[\mathrm{adp}]$ becomes lower than a certain threshold during the relaxation, the corresponding trajectory takes a detour way to the attractor comparing other trajectories that $[\mathrm{atp}]+[\mathrm{adp}]$ is higher than the threshold value (see *SI Text* Section.5).

The robustness of the emergence of distinct trajectories to the parameter values was also examined. For several values of the total adenine nucleotide carriers concentration (A_t), we randomly assigned the rate constant (v_i) and the irreversibility constant (k_i) of each reaction (Eq.[3]) and checked if the distribution of the expansion ratio is multimodal. The multimodality was robust to the parameter choice, and as expected from the analysis, the total concentration, A_t is an important parameter. If A_t is too large as the depletion of ATP and ADP hardly occurs, the expansion ratio becomes unimodal (*SI Text* Section.11). It is checked that the model without the replacement of the nicotinamide nucleotide carriers by the adenine nucleotide carriers exhibits distinct trajectories (*SI text* Section.9). Also, we have confirmed that the distinct trajectories emerge if the assumption on the total concentration of the adenine nucleotide carriers is relaxed by introducing a phenomenological reaction for the de-novo synthesis of AMP to the minimal model (*SI Text* Section.8).

The present study was motivated by a naïve question: what happens if the concentrations of the cofactors are also introduced in the kinetic model of *E. coli* central carbon metabolism. As we saw, it led to the emergence of the distinct trajectories, and the necessity of the cofactors to the phenomenon is well highlighted by the result of model reduction and additional analysis presented in *SI Text*: all the minimal model obtained from random orders of reaction removal keep ATP, ADP, and AMP (Section.10), the importance of the total concentration of ATP and ADP for discriminating the trajectories (Section.3), and the dependency of the fraction of parameter sets leading to distinct trajectories on A_t (Section.11).

If one is interested in the fitting and the prediction of a typical cellular behavior in the log phase as most of the previous works using kinetic models were aiming at (21–31), the dormant dynamics is not of one's interest because of the extremely slow growth rate during the relaxation. In addition, a huge range of the concentrations of chemicals in the dormant trajectories results in the heavy computational burden. These two points are possibly main reasons of why previous models did not include the dynamics of cofactors (21–31) or dynamics were not actually computed (32–36). However, the present study and recent experimental reports taken together imply

DRAFT

bioRxiv preprint doi: https://doi.org/10.1101/2021.07.21.453212; this version posted July 21, 2021. The copyright holder for this preprint (which was not certified by peer review) is the author/funder, who has granted bioRxiv a license to display the preprint in perpetuity. It is made available under aCC-BY-ND 4.0 International license.

that the dormant dynamics is not just an useless artifact with a computational burden, but may reflects the nature of bacterial physiology.

Indeed, slow growths and low metabolic activities that the dormant trajectories exhibit are parts of the characteristic nature of the bacterial persistence (5, 11, 12, 14, 41). Interestingly, recent studies shed light on the relationship of the persister formation to the ATP depletion, not only in *E.coli* (42, 43), but also in a Gram-positive bacterium *Staphylococcus aureus* (44, 45). Further, Radzikowski et. al suggested that the persister formation in *E.coli* was triggered first by a strong perturbation of metabolic state: metabolism is autonomous system in a sense that it generates, and at the same time, is driven by chemical energy. Thus, a collapse of metabolic homeostasis prohibits restoring the homeostasis. This vicious state may be stabilized by ppGpp, Toxin-Antitoxin modules, and the σ^S-mediated stress responses (41). In addition, Mok et. al showed that *E. coli* populations exhibit high persister fractions and the accumulation of all four ribonucleotide monophosphates, including AMP, by inducing the expression of one of the toxin genes, MazF, known to lead to RNA futile cycles consuming the nucleotide triphosphates such as ATP (46).

One of the advantages of the model reduction method developed in this work is that we can find the counterpart of the reactions in the minimal model in the full *E.coli* metabolic network because we never merged any reactions but simply removed them. The central part of the mechanism is that PPS and PYK can form the futile cycle and the competition between PPS and ADK1 on the consumption/production of ATP. Indeed, the experiments showed that one can induce the ATP-consuming futile cycle between phosphoenolpyruvate and pyruvate via PYK and PPS by overexpressing the ppsA gene (47, 48). Taken the experimental reports and the present computational results together, we can hypothesize that the overexpression of the pps gene leads to an increase of the persister fraction because PPS coverts ATP to AMP.

Lastly, we like to remark that the model reduction method developed in the present manuscript can be applied also for the metabolic models of other organisms. We can find several reactions which potentially form a futile cycle from a variety of species. For instance, each of Acetyl-CoA synthetase (KEGGID:R00235), Phosphoribosylpyrophosphate synthetase (R01049) and Asparagine synthase (R00578) (49) converts ATP to AMP and forms a loop in the metabolic networks. These are the minimum requirements for a reaction to form a futile cycle discussed above. Such reactions are widespread from prokaryote to eukaryote, and from unicellular to multicellular organisms. Comprehensive studies of the kinetic models of not only *E. coli* but also other organisms may pave a way for understanding the robust and generic network features leading to the multiple timescales of cellular growth and dormancy.

Acknowledgments

The authors thank Chikara Furusawa and Sandeep Krishna for fruitful discussion. This work is supported by the research grant (00028054) from VILLUM FONDEN.

Materials and Methods

Simulation of ordinary differential equations (ODEs). All the ODE computations were performed by using Matlab (Mathworks) `ode23s` function. Initial values of the concentrations of the chemicals are given as 10^u where u is the random number generated from a uniform distribution in $[-1, 1]$. The ODEs were computed with two tolerance options ($\texttt{AbsTol} = 10^{-10}, \texttt{RelTol} = 10^{-12}$) and ($\texttt{AbsTol} = 10^{-10}, \texttt{RelTol} = 10^{-14}$) from exactly the same initial points. After the computation, the trajectories with two different `RelTol` values, but from the same initial point were compared for the quality check of the computation. If the Hausdorff distance of the pair of the trajectories was less than 0.5, the trajectories were considered as correctly computed and the trajectory obtained with $\texttt{RelTol} = 10^{-14}$ was used for the further analysis, and otherwise, discarded. The quality check of the computation was performed after the transformation $x(t) \to \ln(x(t))$ where $x(t)$ is the concentration of the chemicals.

Hausdorff distance. Hausdorff distance is computed by using the python package `scipy.spatial.distance.directed_hausdorff` as the maximum of two directed Hausdorff distances after the transformation of concentration into the natural logarithm of the concentration.

Principal Component Analysis. We used the python package `sklearn.decomposition.PCA` (50) without whitening. The whitening leads to only a minor effect on the results. The concentrations of the chemicals were transformed into the natural logarithm of the concentration before the analysis.

1. G Sezonov, D Joseleau-Petit, R d'Ari, Escherichia coli physiology in luria-bertani broth. *J. bacteriology* **189**, 8746–8749 (2007).
2. DA Gray, et al., Extreme slow growth as alternative strategy to survive deep starvation in bacteria. *Nat. communications* **10**, 1–12 (2019).
3. DL Kirchman, XAG Morán, H Ducklow, Microbial growth in the polar oceans—role of temperature and potential impact of climate change. *Nat. Rev. Microbiol.* **7**, 451–459 (2009).
4. TJ Strovas, LM Sauter, X Guo, ME Lidstrom, Cell-to-cell heterogeneity in growth rate and gene expression in methylobacterium extorquens am1. *J. bacteriology* **189**, 7127–7133 (2007).
5. NQ Balaban, J Merrin, R Chait, L Kowalik, S Leibler, Bacterial persistence as a phenotypic switch. *Science* **305**, 1622–1625 (2004).
6. M Schaechter, JP Williamson, JH Jun, AL Koch, Growth, cell and nuclear divisions in some bacteria. *Microbiology* **29**, 421–434 (1962).
7. P Wang, et al., Robust growth of escherichia coli. *Curr. biology* **20**, 1099–1103 (2010).
8. Y Wakamoto, J Ramsden, K Yasuda, Single-cell growth and division dynamics showing epigenetic correlations. *Analyst* **130**, 311–317 (2005).
9. EJ Stewart, R Madden, G Paul, F Taddei, Aging and death in an organism that reproduces by morphologically symmetric division. *PLoS biology* **3**, e45 (2005).
10. M Hashimoto, et al., Noise-driven growth rate gain in clonal cellular populations. *Proc. Natl. Acad. Sci.* **113**, 3251–3256 (2016).
11. E Kussell, R Kishony, NQ Balaban, S Leibler, Bacterial persistence: a model of survival in changing environments. *Genetics* **169**, 1807–1814 (2005).
12. NQ Balaban, et al., Definitions and guidelines for research on antibiotic persistence. *Nat. Rev. Microbiol.* **17**, 441–448 (2019).
13. JW Veening, WK Smits, OP Kuipers, Bistability, epigenetics, and bet-hedging in bacteria. *Annu. Rev. Microbiol.* **62**, 193–210 (2008).
14. K Lewis, Persister cells. *Annu. review microbiology* **64**, 357–372 (2010).
15. S Klumpp, Z Zhang, T Hwa, Growth rate-dependent global effects on gene expression in bacteria. *Cell* **139**, 1366–1375 (2009).
16. O Kotte, B Volkmer, JL Radzikowski, M Heinemann, Phenotypic bistability in escherichia coli's central carbon metabolism. *Mol. systems biology* **10**, 736 (2014).
17. C Tan, P Marguet, L You, Emergent bistability by a growth-modulating positive feedback circuit. *Nat. chemical biology* **5**, 842–848 (2009).
18. L Riber, LH Hansen, Epigenetic memories: The hidden drivers of bacterial persistence? *Trends Microbiol.* (2021).
19. A Awazu, K Kaneko, Ubiquitous "glassy" relaxation in catalytic reaction networks. *Phys. Rev. E* **80**, 041931 (2009).
20. A Awazu, K Kaneko, Discreteness-induced slow relaxation in reversible catalytic reaction networks. *Phys. Rev. E* **81**, 051920 (2010).
21. C Chassagnole, N Noisommit-Rizzi, JW Schmid, K Mauch, M Reuss, Dynamic modeling of the central carbon metabolism of escherichia coli. *Biotechnol. bioengineering* **79**, 53–73 (2002).
22. H Kurata, Y Sugimoto, Improved kinetic model of escherichia coli central carbon metabolism in batch and continuous cultures. *J. bioscience bioengineering* **125**, 251–257 (2018).

DRAFT

bioRxiv preprint doi: https://doi.org/10.1101/2021.07.21.453212; this version posted July 21, 2021. The copyright holder for this preprint (which was not certified by peer review) is the author/funder, who has granted bioRxiv a license to display the preprint in perpetuity. It is made available under aCC-BY-ND 4.0 International license.

23. TAA Kadir, AA Mannan, AM Kierzek, J McFadden, K Shimizu, Modeling and simulation of the main metabolism in escherichia coli and its several single-gene knockout mutants with experimental verification. *Microb. cell factories* **9**, 1–21 (2010).
24. Y Tohsato, K Ikuta, A Shionoya, Y Mazaki, M Ito, Parameter optimization and sensitivity analysis for large kinetic models using a real-coded genetic algorithm. *Gene* **518**, 84–90 (2013).
25. O Kotte, JB Zaugg, M Heinemann, Bacterial adaptation through distributed sensing of metabolic fluxes. *Mol. systems biology* **6**, 355 (2010).
26. K Peskov, E Mogilevskaya, O Demin, Kinetic modelling of central carbon metabolism in escherichia coli. *The FEBS journal* **279**, 3374–3385 (2012).
27. AA Mannan, et al., Integrating kinetic model of e. coli with genome scale metabolic fluxes overcomes its open system problem and reveals bistability in central metabolism. *PloS one* **10**, e0139507 (2015).
28. J Di Maggio, JD Ricci, MS Diaz, Global sensitivity analysis in dynamic metabolic networks. *Comput. & Chem. Eng.* **34**, 770–781 (2010).
29. K Bettenbrock, et al., A quantitative approach to catabolite repression in escherichia coli. *J. Biol. Chem.* **281**, 2578–2584 (2006).
30. VK Singh, I Ghosh, Kinetic modeling of tricarboxylic acid cycle and glyoxylate bypass in mycobacterium tuberculosis, and its application to assessment of drug targets. *Theor. Biol. Med. Model.* **3**, 1–11 (2006).
31. CJ TORRES, V Guixé, J Babul, A mutant phosphofructokinase produces a futile cycle during gluconeogenesis in escherichia coli. *Biochem. J.* **327**, 675–684 (1997).
32. Y Tan, JC Liao, Metabolic ensemble modeling for strain engineers. *Biotechnol. journal* **7**, 343–353 (2012).
33. LM Tran, ML Rizk, JC Liao, Ensemble modeling of metabolic networks. *Biophys. journal* **95**, 5606–5617 (2008).
34. A Khodayari, AR Zomorrodi, JC Liao, CD Maranas, A kinetic model of escherichia coli core metabolism satisfying multiple sets of mutant flux data. *Metab. engineering* **25**, 50–62 (2014).
35. A Khodayari, CD Maranas, A genome-scale escherichia coli kinetic metabolic model k-ecoli457 satisfying flux data for multiple mutant strains. *Nat. communications* **7**, 1–12 (2016).
36. ML Rizk, JC Liao, Ensemble modeling for aromatic production in escherichia coli. *PloS one* **4**, e6903 (2009).
37. TS Hatakeyama, C Furusawa, Metabolic dynamics restricted by conserved carriers: Jamming and feedback. *PLoS computational biology* **13**, e1005847 (2017).
38. PB Orth J, Fleming R, *Reconstruction and Use of Microbial Metabolic Networks: the Core Escherichia coli Metabolic Model as an Educational Guide*. (2010).
39. ZA King, et al., Escher: a web application for building, sharing, and embedding data-rich visualizations of biological pathways. *PLoS Comput. Biol* **11**, e1004321 (2015).
40. A Cornish-Bowden, *Fundamentals of enzyme kinetics*. (John Wiley & Sons), (2013).
41. JL Radzikowski, et al., Bacterial persistence is an active σs stress response to metabolic flux limitation. *Mol. systems biology* **12**, 882 (2016).
42. S Manuse, et al., Bacterial persisters are a stochastically formed subpopulation of low-energy cells. *PLoS biology* **19**, e3001194 (2021).
43. Y Shan, et al., Atp-dependent persister formation in escherichia coli. *MBio* **8** (2017).
44. BP Conlon, et al., Persister formation in staphylococcus aureus is associated with atp depletion. *Nat. microbiology* **1**, 1–7 (2016).
45. EA Zalis, et al., Stochastic variation in expression of the tricarboxylic acid cycle produces persister cells. *MBio* **10** (2019).
46. WW Mok, JO Park, JD Rabinowitz, MP Brynildsen, Rna futile cycling in model persisters derived from mazf accumulation. *MBio* **6**, e01588–15 (2015).
47. R Patnaik, W Roof, R Young, J Liao, Stimulation of glucose catabolism in escherichia coli by a potential futile cycle. *J. bacteriology* **174**, 7527–7532 (1992).
48. O Hädicke, K Bettenbrock, S Klamt, Enforced atp futile cycling increases specific productivity and yield of anaerobic lactate production in escherichia coli. *Biotechnol. bioengineering* **112**, 2195–2199 (2015).
49. M Kanehisa, S Goto, Kegg: kyoto encyclopedia of genes and genomes. *Nucleic acids research* **28**, 27–30 (2000).
50. F Pedregosa, et al., Scikit-learn: Machine learning in Python. *J. Mach. Learn. Res.* **12**, 2825–2830 (2011).

DRAFT